JPhys Energy

PAPER

Formation of stable 2D methylammonium antimony iodide phase for lead-free perovskite-like solar cells*

Nadja Giesbrecht[1], **Andreas Weis**[1] **and Thomas Bein**[2]

Department of Chemistry and Center for NanoScience (CeNS), University of Munich (LMU), Butenandtstr. 5-13, D-81377 München, Germany

[1] Contributed equally to this work.

[2] Author to whom any correspondence should be addressed.

E-mail: bein@lmu.de

Keywords: photovoltaics, antimony, lead-free, perovskite-like, 2D

Supplementary material for this article is available online

OPEN ACCESS

RECEIVED
22 November 2019

REVISED
19 February 2020

ACCEPTED FOR PUBLICATION
21 February 2020

PUBLISHED
20 March 2020

Abstract

The presence of lead in novel hybrid perovskite-based solar cells remains a significant issue regarding commercial applications. Therefore, antimony-based perovskite-like $A_3M_2X_9$ structures are promising new candidates for low toxicity photovoltaic applications. So far, $MA_3Sb_2I_9$ was reported to only crystallize in the 'zero-dimensional' (0D) dimer structure with wide indirect bandgap properties. However, the formation of the 2D layered polymorph is more suitable for solar cell applications due to its expected direct and narrow bandgap. Here, we demonstrate the first synthesis of phase pure 2D layered $MA_3Sb_2I_9$, based on antimony acetate dissolved in alcoholic solvents. Using *in situ* XRD methods, we confirm the stability of the layered phase towards high temperature, but the exposure to 75% relative humidity for several hours leads to a rearrangement of the phase with partial formation of the 0D structure. We investigated the electronic band structure and confirmed experimentally the presence of a semi-direct bandgap at around 2.1 eV. Our work shows that careful control of nucleation via processing conditions can provide access to promising perovskite-like phases for photovoltaic applications.

Introduction

The hybrid lead halide perovskite material methylammonium lead iodide ($MAPbI_3$) emerged with an initial photovoltaic performance of 3.8% in 2009 [1]. Today, the solar cell efficiencies using $MAPbI_3$-based absorbers already exceed 25% due to the material's intrinsic outstanding optoelectronic properties [2]. In particular, lead-based perovskites exhibit high optical absorption coefficients, balanced electron and hole mobilities, long photogenerated carrier lifetimes, long diffusion lengths, low trap densities and small exciton binding energies [3–8]. These exceptional material properties originate from a combination of high crystal symmetry, the chemistry of the Pb $6s^2$ lone-pair states and the ionic nature of the structure with large atomic sizes [9]. However, the toxicity of lead together with the instability of this and related perovskite compounds towards moisture and high temperature limit the commercialization of lead-based perovskite solar cells [10–14].

To find alternatives replacing lead, researchers have focused on other isovalent ions, like Sn^{2+} or Ge^{2+}. Here, both $MASnI_3$ and $MAGeI_3$ are suitable candidates for photovoltaic applications due to a possible crystallization in a black perovskite crystalline phase [15–23]. Unfortunately, the divalent ions in tin- and germanium-based perovskites are prone to oxidize to Sn^{4+} or Ge^{4+}, respectively. Therefore, these absorbers are especially unstable in air and moisture, limiting their photovoltaic applications [20, 24, 25].

Maintaining the chemistry of the lone-pair ns^2 state, the trivalent antimony and bismuth ions represent another possible alternative to replace lead. However, the higher oxidation state of antimony or bismuth compared to lead in $MAPbI_3$ makes similar perovskite phase formation impossible. Instead, $MA_3Sb_2I_9$ or

* Dedicated to Dr Klaus Römer on the occasion of his 80th birthday.

$MA_3Bi_2I_9$ form. The methylammonium-based compounds crystallize predominantly in a non-perovskite, zero-dimensional (0D) phase, consisting of face-sharing bioctahedral clusters of $(Sb_2I_9)^{3-}$ or $(Bi_2I_9)^{3-}$. The antimony-based absorber layers crystallize in high quality with extended HI treatment [26]. If applied in solar cells, those layers enable power conversion efficiencies (PCEs) of 2% and can be further improved to 2.8% efficiency with a hydrophobic scaffold at the bottom interlayer [26, 27]. The already promising photovoltaic performance indicates the suitability of $MA_3Sb_2I_9$ as an absorber layer, even though the 0D structure exhibits neither a direct bandgap nor interconnected octahedral layers for charge transport in any dimension.

In density functional theory (DFT) calculations, $MA_3Sb_2I_9$ (MASI) features more favorable materials properties when crystallized in a layered 2D structure. The projected improved materials properties include a direct bandgap, higher electron and hole mobilities and better tolerance to defects caused by higher dielectric constants [26, 28–30]. However, the crystallization of the layered phase preferably occurs with smaller cations than MA^+, such as Rb^+ or NH_4^+ [31–33]. Absorber layers based on $Rb_3Sb_2I_9$ and $(NH_4)_3Sb_2I_9$ exhibit a direct bandgap and reach PCEs of 0.7% and 0.5%, respectively [32, 33]. Introduction of bulkier Cs^+ cations in the layered 2D structure requires more extended processing conditions, such as recrystallization of the dimer phase in SbI_3 vapor [30]. Exhibiting a direct bandgap, $Cs_3Sb_2I_9$ enables a PCE of 1.5% [30]. With MA^+ as a cation, so far, layered $MA_3Sb_2I_{9-x}Cl_x$ could only be achieved via partial anion substitution using the smaller anion Cl^- [34]. In devices, high quality 2D thin films achieved a PCE of 2.2%, but the slightly wider bandgap of 2.17 eV suggests that even higher efficiencies could arise from a material with a narrower bandgap [34].

In this work, we present a novel synthesis approach based on antimony acetate precursor to crystallize a pure $MA_3Sb_2I_9$ 2D perovskite-like phase. We perform solvent-engineering to induce the crystallization of the layered structure, confirmed with XRD and UV–vis analysis. Further investigations using *in situ* XRD proved the stability of the material toward phase transition and degradation upon exposure to heat and substantially to moisture. In first-principles calculations, we predict a semi-direct bandgap of the 2D compound and confirm these results with optical absorbance spectroscopy, showing a direct bandgap of 2.1 eV. Even though we fabricated rather low-quality thin film morphologies of MASI, devices reach already PCEs around 0.6%, indicating the materials' aptness for photovoltaic applications.

Results and discussion

The two known phases of MASI differ significantly, considering the crystal structure. The dimer phase, as explained above, consists of face-sharing $(Sb_2I_9)^{3-}$ bioctahedral clusters with MA^+ and iodide, forming a quasi-hexagonal close packing [35]. In this structure, the closest Sb–Sb interatomic distance is 4.1 Å. Increasing the range of antimony-iodide octahedra such that the antimony atoms are separated by 4.8 Å, MASI forms in the layered structure with corner-sharing octahedral. The MA- and I-ions form a quasi-cubic close packing. This 2D phase can be understood as a defective $MAPbI_3$-like perovskite structure with the formula $MA(Sb_{2/3}\square_{1/3})I_3$. However, the 2D structure predominantly forms with smaller cations than MA^+. Regarding literature results, only SbI_3 was utilized as an antimony precursor in the different syntheses, with 4.4 Å separating the antimony atoms surrounded octahedrally by iodide. Therefore, only small cations like Rb^+ and NH_4^+ seem to easily squeeze between the octahedra in SbI_3 to form the layered phase and larger cations instead push the octahedra closer towards the dimer phase, as illustrated in figure 1. Thus, we considered the antimony acetate precursor. In $Sb(OAc)_3$, antimony is coordinated with seven oxygen atoms, leading to a separation of 4.9 Å between the closest antimony atoms. We suggest that with the introduction of MA- and I-ions to $Sb(OAc)_3$, antimony iodide octahedra form with MA^+ fitted in between, resulting in the 2D-MASI phase (see figure 1). With powder XRD analysis, we confirm the successful synthesis of thin films of 2D-MASI, view supporting information (SI), available online at stacks.iop.org/JPENERGY/2/024007/mmedia. The resulting crystal structure strongly agrees with the simulated pattern of the material. Only small amounts of an additional dimer phase are visible.

For the formation of the 2D-MASI phase from antimony acetate precursor, the nature of the solvent is decisive. Using dimethylformamide (DMF), the dimer phase forms predominantly with traces of the layered phase, see supporting information (SI). Solvents containing sulfur leading to a strong interaction with antimony, like dimethylsulfoxide (DMSO) or tetrahydrothiophene-1-oxide (THTO), induce phase pure dimer phase crystallization (see SI) [36]. However, solvents based on alcohols are highly suitable for MASI formation in the 2D phase, with best results observed when using methanol (MeOH). Please see SI for more details on exact thin film synthesis details. During MASI thin-film crystallization from MeOH, the annealing temperature is decisive for the phase formation. With annealing temperatures below 100 °C, the crystallization process slows down, which correlates with added dimer formation (see SI). Therefore, we suggest a fast crystallization process to form MASI in the layered phase and not in the more thermodynamically preferred dimer phase.

Other alcohols such as ethanol (EtOH) also induce 2D phase formation of MASI from antimony acetate precursor (see SI). However, the solubility decreases dramatically to a concentration of 0.125 mmol $Sb(OAc)_3$ in

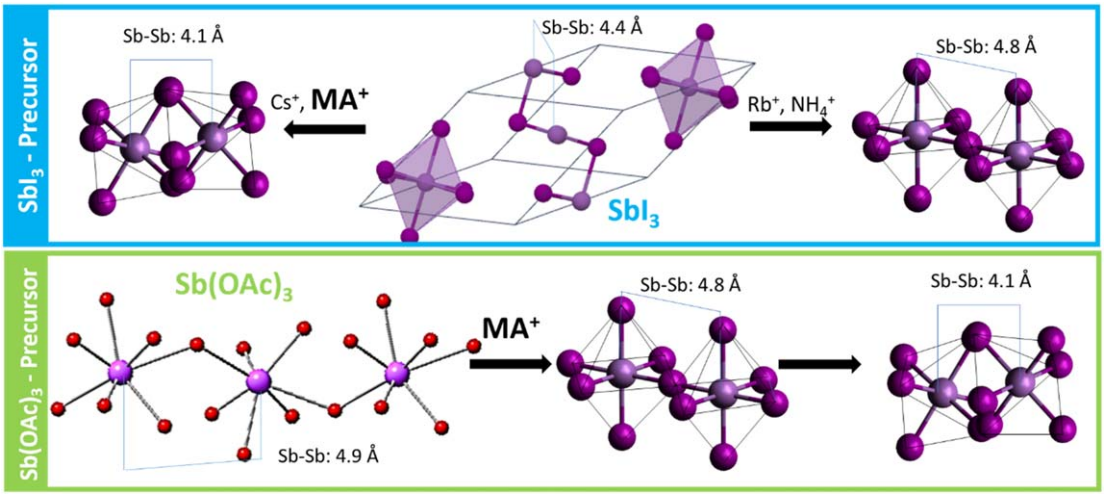

Figure 1. Schematic illustration of polyhedra arrangement in different antimony precursors and 0D-, 2D-MASI phase.

1 ml EtOH. Therefore, alcohols with longer organic chains like isopropanol (IPA) are not suitable for the synthesis. If not otherwise stated, in the following, we always refer to the 2D-MASI compound prepared from MeOH.

Other than structural differences, the dimer and the layered MASI phases are clearly distinguished by their optoelectronic properties. The most significant divergence lies in the nature and width of the semiconductor's bandgap. To predict the electronic band structure of the 0D and 2D-MASI phases, we performed first-principles calculations using plane-wave pseudopotential methods within DFT as implemented in the Quantum Espresso Package [37]. For the sake of computational efficiency, all calculations were carried out with the Cs-cation since the organic cation shows no influence regarding the frontier electronic band structure [38, 39]. Neglecting the well-known deficiency of the gradient corrected method Perdew–Burke–Enzerhof functional to estimate the magnitude of the bandgap, the indirect nature of the bandgap is more strongly pronounced for the dimer phase compared to the layered phase, see SI figure 3 [40]. The more pronounced indirect bandgap characteristics most probably arise from the lower crystal lattice symmetry of the 0D polymorph in comparison with the 2D phase [34]. Additionally, the very flat band determined by the valence band maximum of the 2D phase indicates a quasi-direct-indirect transition, seen in the X $\rightarrow$ Y path in the Brillouin zone (see SI figure 3).

To verify our theoretical calculations, we characterized our MASI films via UV–vis absorbance spectroscopy. Based on the absorbance spectra in figure 2(a), we observed the onset at longer wavelengths with the layered phase indicating a narrower bandgap compared to the dimer phase. Furthermore, calculated Tauc plots from the data of the layered material show a direct transition at 2.1 eV and an indirect transition at 2.0 eV, supporting the theoretical expectations and verifying the phase purity of 2D-MASI (see figure 2(b)). In principle, materials benefiting from both direct and indirect bandgap behavior are favorable candidates for photovoltaic applications. Usually, strong absorption is coupled with a direct bandgap and long carrier lifetime with an indirect band-to-band transition, similar to what was observed in $MAPbI_3$ [41]. We note, that films synthesized from EtOH instead of MeOH indicate two onsets in the absorbance spectrum in SI figure 1(c), implying a 2D and 0D phase mixture.

Additional to the nature of the bandgap, the exciton binding energy E_b in a material determines the suitability of the compound for photovoltaic applications. Here, the minima in the second derivative of the absorbance can be used to estimate E_b [42]. Our results, displayed in table 1, show that compared to $MAPbI_3$, the exciton binding energy values in MASI thin films are one order of magnitude higher [42]. However, our 2D-MASI films show significantly weaker exciton binding compared to the reported and our experimentally obtained values for the 0D-MASI films [43]. To understand the influence of the exciton binding energy on carrier dynamics, we employed a numerical method based on the Saha equation, described in detail in SI [42]. Figure 2(d) shows the results from the extracted data with a range of typical values reported for solar cell absorbers for total excitation density marked in an orange box [42]. With the dimer MASI phase the excitonic contribution is dominant in contrast to what we observed with our 2D-MASI thin films. Regarding the layered phase, the more desirable balanced contribution of free charge carriers and excitons is evident. Therefore, the layered MASI phase appears to be more suitable for photovoltaic applications compared to its 0D polymorph.

In addition to the optoelectronic properties of the materials, the stability of the compounds is crucial to consider their suitability for photovoltaic applications. Solar cells operate at temperatures of up to 85 °C and

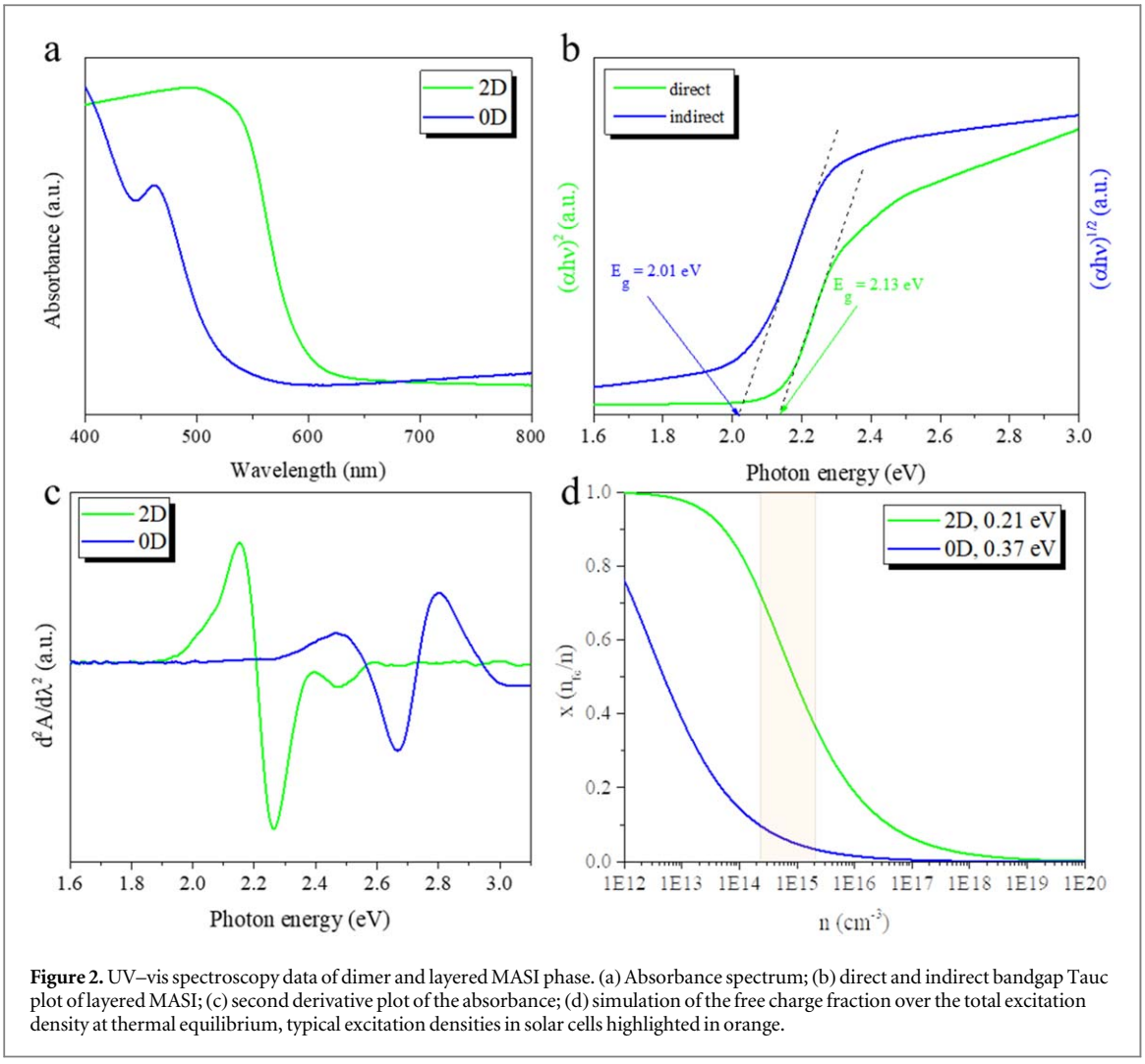

Figure 2. UV–vis spectroscopy data of dimer and layered MASI phase. (a) Absorbance spectrum; (b) direct and indirect bandgap Tauc plot of layered MASI; (c) second derivative plot of the absorbance; (d) simulation of the free charge fraction over the total excitation density at thermal equilibrium, typical excitation densities in solar cells highlighted in orange.

Table 1. Exciton binding energies estimated from the second derivative of the absorbance.

	First minimum (eV)	Second minimum (eV)	E_b (eV)
2D-MASI	2.26	2.47	0.21
0D-MASI	2.66	3.03	0.37

degradation of the absorber material can, therefore, be a concern. In figure 3(a), we show an *in situ* XRD analysis conducted at 80 °C for one hour and afterward at 130 °C for one hour. We analyzed the powder obtained from the thin-film synthesis of the 2D-MASI phase to emphasize the substantially higher stability of the compound. The analysis of the powder in contrast to thin films additionally avoids the extinction of reflexes due to preferred crystal alignment and therefore highlights here the presence of pure 2D-MASI phase, differing from the 0D-MASI phase with an additional peak at around 27°. Neither a phase transition to the dimer phase nor decomposition is evident in our study. The only apparent change in the high temperature investigations is the shift of the reflections to lower 2θ angles indicating an increase of the unit cell dimensions in the layered structure similar to the observations for $MAPbI_3$ [44]. The increase of the unit cell dimensions is reversible, as demonstrated by the shift of the reflections to their original positions at higher 2θ angles after cooling.

Another essential factor concerning the stability of the material is its sensitivity towards moisture. Therefore, we performed an *in situ* XRD analysis at temperatures between 27 °C and 31 °C under 75% relative humidity conditions (see figure 3(b)). Under these harsh conditions, our pristine layered MASI films partly recrystallized to the zero-dimensional phase after 10 h. In the course of further tracing the phase transition, we found a complete transformation to the dimer phase after 50 h. Further continuous moisture exposure for one week results in an oxidized antimony-containing phase as confirmed via energy dispersive X-ray analysis, shown in

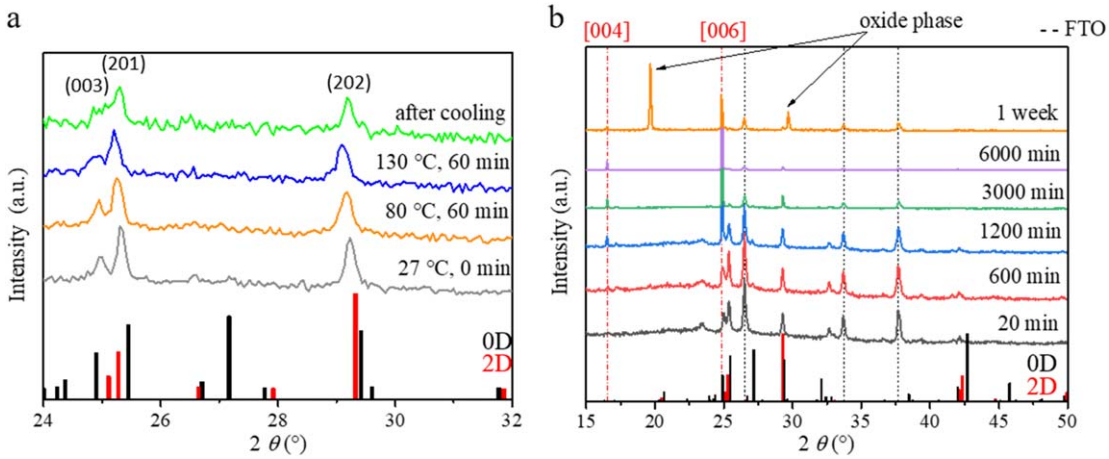

Figure 3. *In situ* XRD analysis of 2D-MASI. (a) Analysis of powder at high temperatures with marked prominent reflection indexes; (b) analysis of thin films at 75% relative humidity at temperatures between 27 °C and 31 °C.

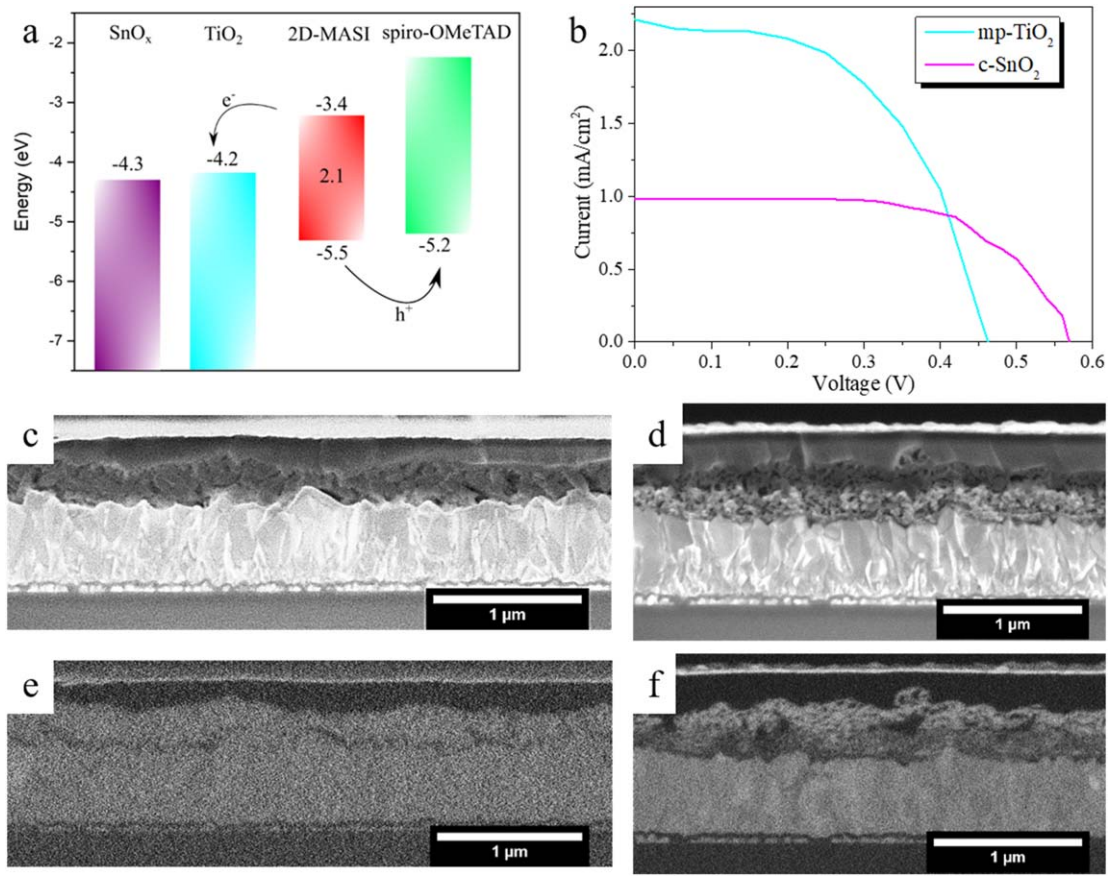

Figure 4. Photovoltaic devices with 2D-MASI absorber layer sandwiched between FTO/metal-oxide electron transport layer and the hole-transporter spiro-OMeTAD/Au. (a) Schematic illustration of energy levels of SnO_2, TiO_2, 2D-MASI and spiro-OMeTAD; (b) *JV*-curves of devices with mp-TiO_2 or c-SnO_2 as ETL; (c) + (e) SEM cross-section of devices with SnO_2 ETL with (top) topography sensitive secondary electrons detector and (bottom) mass sensitive detector; (d) + (f) SEM cross-section of devices with mp-TiO_2 ETL with (top): topography sensitive detector and (bottom) mass sensitive backscattered-electron detector.

the SI. The observed instability towards moisture of the MASI compound is much less pronounced than that of $MAPbI_3$ [13]. Studies with much thinner 2D-MASI films obtained from EtOH show that the sensitivity towards moisture becomes more evident, indicating a strong influence of morphology on stability (see SI).

Finally, we applied our novel 2D-MASI absorber layer in photovoltaic devices, using metal oxide as electron transport layers (ETL) and spiro-OMeTAD as a hole-transport layer (HTL). As visible in the schematic in figure 4(a), the energy alignment of the ETL with our absorber layer is not optimal for efficient electron transport

Table 2. Photovoltaic parameters of the fabricated solar cells from figure 4.

ETL	Current density (mA cm^{-2})	PCE (%)	Voltage (V)	Fill factor (%)
Meso-TiO_2	2.21	0.54	0.46	52
c-SnO_2	0.98	0.36	0.57	64

and other device architectures are required. The thin film morphologies of the MASI layer, shown in the SEM top-views in SI and SEM cross-sections of devices in figure 4, are also not yet optimized with their low crystallinity and voids highly pronounced at ETL and absorber interface. However, even under these limiting conditions, devices reach already PCEs of around 0.6%. Devices with a mesoporous (mp-) TiO_2 as ETL perform best (see table 2), highlighting the strong correlation of absorber layer morphology with photovoltaic performance. In general, the phase pure 2D-MASI films obtained from MeOH solvent reach higher efficiencies compared to the less stable and less phase pure films from EtOH solvent synthesized under similar conditions (see SI figure 5(b)). Similar to their hybrid lead halide relatives, MASI-based devices show high hysteresis in *JV*-scans [45]. Only with SnO_x as ETL, we observed no pronounced hysteresis between forward and reverse scans (see SI figure 5(a)) and improved values for fill factor and voltage but significantly low current density values (see table 2 and SI). Additionally, the photovoltaic device performance using compact SnO_2 as ETM is more reproducible than that of the higher-performing mp-TiO_2 devices, see SI figure 6. In particular, the lower current density limits the device performance distinctly, using planar device architectures. Thus, we suggest that high defect densities in the material due to the not densely-packed nanocrystalline MASI thin film morphologies are responsible for the low photovoltaic efficiencies. Assuming internal quantum efficiencies near unity as observed in $MAPbI_3$-based solar cells, possible current densities based on our thin-film absorption are around 9 mA cm^{-2} (see SI figure 1(d)) [46]. In combination with a voltage of 1 V, which is defined by the energy level alignment of the HTL and ETLs used in this work, device efficiencies of around 6% are probable. With more optimized device architectures, the photovoltaic performance might even exceed 10% if higher voltages with the wide bandgap material can be obtained.

Conclusion

In summary, we report the first synthesis of pure $MA_3Sb_2I_9$ crystallized in a layered perovskite-like phase. Here, the use of the antimony acetate precursor is crucial for a fast 2D-MASI formation with the sustainable solvents MeOH or EtOH. Our theoretical calculations and experimental investigations agree regarding a semi-direct nature of the bandgap in the 2D material, in contrast to the strongly indirect bandgap of the 0D compound. Additionally, we find considerably weaker excitonic binding energies in 2D-MASI compared to the 0D polymorph, which is desirable for photovoltaic applications. At high temperatures, the 2D-MASI phase remains stable. However, at this point, the inhomogeneous thin film morphology limits the stability of 2D-MASI at high humidity levels and probably is responsible for the limited photovoltaic device performance. Therefore, we expect that with further optimized thin film morphologies, 2D-MASI is a promising new candidate for lead-free photovoltaic applications.

Acknowledgments

This work was supported by the Deutsche Forschungsgemeinschaft (DFG, Excellence clusters NIM and e-conversion), the Bavarian State Ministry for Sciences, Research and the Arts with the network Solar Technologies go Hybrid (SolTech) and the Center for NanoScience (CeNS).

ORCID iDs

Nadja Giesbrecht https://orcid.org/0000-0002-1183-4129

References

[1] Kojima A, Teshima K, Shirai Y and Miyasaka T 2009 *J. Am. Chem. Soc.* **131** 6050–1
[2] NREL 2020 Research Cell Record Efficiency Chart (www.nrel.gov/pv/assets/pdfs/best-research-cell-efficiencies.20200218.pdf)
[3] Xing G, Mathews N, Sun S, Lim S S, Lam Y M, Grätzel M, Mhaisalkar S and Sum T C 2013 *Science* **342** 344–7
[4] Eperon G E, Stranks S D, Menelaou C, Johnston M B, Herz L M and Snaith H J 2014 *Energy Environ. Sci.* **7** 982–8
[5] Wehrenfennig C, Eperon G E, Johnston M B, Snaith H J and Herz L M 2014 *Adv. Mater.* **26** 1584–9

[6] Edri E, Kirmayer S, Henning A, Mukhopadhyay S, Gartsman K, Rosenwaks Y, Hodes G and Cahen D 2014 *Nano Lett.* **14** 1000–4
[7] Wang J T-W *et al* 2016 *Energy Environ. Sci.* **9** 2892–901
[8] Yin W-J, Shi T and Yan Y 2014 *Adv. Mater.* **26** 4653–8
[9] Yin W-J, Shi T and Yan Y 2015 *J. Phys. Chem.* C **119** 5253–64
[10] Flora G, Gupta D and Tiwari A 2012 *Interdiscip. Toxicol.* **5** 47
[11] Fowler B A, Nordberg G F and Nordberg M 2015 *Handbook on the Toxicology of Metals* 4th edn (Amsterdam: Elsevier)
[12] Needleman H 2004 *Annu. Rev. Med.* **55** 209–22
[13] Petrus M L, Hu Y, Moia D, Calado P, Leguy A M A, Barnes P R F and Docampo P 2016 *ChemSusChem* **9** 2699–707
[14] Conings B *et al* 2015 *Adv. Energy Mater.* **5** 1500477
[15] Zhou Y, Garces H F, Senturk B S, Ortiz A L and Padture N P 2013 *Mater. Lett.* **110** 127–9
[16] Chung I, Lee B, He J, Chang R P H and Kanatzidis M G 2012 *Nature* **485** 486
[17] Chung I, Song J-H, Im J, Androulakis J, Malliakas C D, Li H, Freeman A J, Kenney J T and Kanatzidis M G 2012 *J. Am. Chem. Soc.* **134** 8579–87
[18] Marshall K P, Walton R I and Hatton R A 2015 *J. Mater. Chem.* A **3** 11631–40
[19] Stoumpos C C, Malliakas C D and Kanatzidis M G 2013 *Inorg. Chem.* **52** 9019–38
[20] Krishnamoorthy T *et al* 2015 *J. Mater. Chem.* A **3** 23829–32
[21] Liu X, Yan K, Tan D, Liang X, Zhang H and Huang W 2018 *ACS Energy Lett.* **3** 2701–7
[22] Liao W *et al* 2016 *Adv. Mater.* **28** 9333–40
[23] Wang W *et al* 2017 *Adv. Funct. Mater.* **27** 1703953
[24] Leijtens T, Prasanna R, Gold-Parker A, Toney M F and McGehee M D 2017 *ACS Energy Lett.* **2** 2159–65
[25] Stoumpos C C, Frazer L, Clark D J, Kim Y S, Rhim S H, Freeman A J, Ketterson J B, Jang J I and Kanatzidis M G 2015 *J. Am. Chem. Soc.* **137** 6804–19
[26] Boopathi K M, Karuppuswamy P, Singh A, Hanmandlu C, Lin L, Abbas S A, Chang C C, Wang P C, Li G and Chu C W 2017 *J. Mater. Chem.* A **5** 20843–50
[27] Karuppuswamy P, Boopathi K M, Mohapatra A, Chen H-C, Wong K-T, Wang P-C and Chu C-W 2018 *Nano Energy* **45** 330–6
[28] Park B-W, Philippe B, Zhang X, Rensmo H, Boschloo G and Johansson E M J 2015 *Adv. Mater.* **27** 6806–13
[29] Hebig J-C, Kühn I, Flohre J and Kirchartz T 2016 *ACS Energy Lett.* **1** 309–14
[30] Saparov B, Hong F, Sun J-P, Duan H-S, Meng W, Cameron S, Hill I G, Yan Y and Mitzi D B 2015 *Chem. Mater.* **27** 5622–32
[31] Harikesh P C *et al* 2016 *Chem. Mater.* **28** 7496–504
[32] Correa-Baena J-P *et al* 2018 *Chem. Mater.* **30** 3734–42
[33] Zuo C and Ding L 2017 *Angew. Chem. Int. Ed.* **56** 6528–32
[34] Jiang F *et al* 2018 *J. Am. Chem. Soc.* **140** 1019–27
[35] Ju D, Jiang X, Xiao H, Chen X, Hu X and Tao X 2018 *J. Mater. Chem.* A **6** 20753–9
[36] Olivier-Fourcade J, Ibanez A, Jumas J C, Maurin M, Lefebvre I, Lippens P, Lannoo M and Allan G 1990 *J. Solid State Chem.* **87** 366–77
[37] Giannozzi P *et al* 2009 *J. Phys.: Condens. Matter* **21** 395502
[38] Brivio F, Walker A B and Walsh A 2013 *APL Mater.* **1** 042111
[39] Borriello I, Cantele G and Ninno D 2008 *Phys. Rev.* B **77** 235214
[40] Perdew J P, Burke K and Ernzerhof M 1996 *Phys. Rev. Lett.* **77** 3865–8
[41] Hutter E M, Gélvez-Rueda M C, Osherov A, Bulović V, Grozema F C, Stranks S D and Savenije T J 2016 *Nat. Mater.* **16** 115
[42] D'Innocenzo V, Grancini G, Alcocer M J P, Kandada A R S, Stranks S D, Lee M M, Lanzani G, Snaith H J and Petrozza A 2014 *Nat. Commun.* **5** 3586
[43] Scholz M, Morgenroth M, Oum K and Lenzer T 2018 *J. Phys. Chem.* C **122** 5854–63
[44] Ruf F, Aygüler M F, Giesbrecht N, Rendenbach B, Magin A, Docampo P, Kalt H and Hetterich M 2019 *APL Mater.* **7** 031113
[45] Snaith H J, Abate A, Ball J M, Eperon G E, Leijtens T, Noel N K, Stranks S D, Wang J T-W, Wojciechowski K and Zhang W 2014 *J. Phys. Chem. Lett.* **5** 1511–5
[46] Giesbrecht N, Schlipf J, Grill I, Rieder P, Dyakonov V, Bein T, Hartschuh A, Muller-Buschbaum P and Docampo P 2018 *J. Mater. Chem.* A **6** 4822–8